Nuclear Science and Techniques (2024) 35:79
https://doi.org/10.1007/s41365-024-01442-0

Development of a scintillating-fiber-based beam monitor for the coherent muon-to-electron transition experiment

Yu Xu[1] · Yun-Song Ning[1] · Zhi-Zhen Qin[2,3] · Yao Teng[2,3] · Chang-Qing Feng[2,3] · Jian Tang[1] · Yu Chen[1] · Yoshinori Fukao[4] · Satoshi Mihara[4] · Kou Oishi[5]

Received: 12 September 2023 / Revised: 14 November 2023 / Accepted: 20 December 2023 / Published online: 24 May 2024

Abstract
The coherent muon-to-electron transition (COMET) experiment is a leading experiment for the coherent conversion of $\mu^-\mathrm{N} \rightarrow e^-\mathrm{N}$ using a high-intensity pulsed muon beamline, produced using innovative slow-extraction techniques. Therefore, it is critical to measure the muon beam characteristics. We set up a muon beam monitor (MBM), where scintillating fibers woven in a cross shape were coupled to silicon photomultipliers to measure the spatial profile and timing structure of the extracted muon beam for the COMET. The MBM detector was tested successfully with a proton beamline at the China Spallation Neutron Source and took data with good performance in the commissioning run. The development of the MBM, including its mechanical structure, electronic readout, and beam measurement results, are discussed

Keywords Beam instrumentation · Profile monitor · Scintillating fiber · Silicon photomultipliers

1 Introduction

With the steady increase in beam power and intensity required for high-precision measurements in particle and nuclear physics, beam profile monitors play an important role in precisely characterizing beam properties [1–3], especially for real-time control of the beam. The requirements for such a beam profile monitor include fast response, high time resolution, and quasi-noninvasiveness to the beam.

Several types of beam profile monitors are currently available. The most widely used type of beam monitor is the beam position monitor (BPM) used to detect the position of the transverse beam. BPMs can monitor the phase and transverse position of the beam in high-energy particle accelerators by measuring the difference in the total voltage between two opposite pick-ups [4] and come in a wide variety of types, including button BPMs [5], cavity BPMs [6], and stripline BPMs [7]. The other important category of beam monitor is the gas detection system, which is typically based on the gas sheet [8]. Owing to its good stability and noninvasiveness to the beam, the gas detector is widely used for online beam profile measurements, such as the measurement of 400-MeV negative hydrogen atoms in the J-PARC LINAC [9–11], muon beam measurement in NOvA experiments at Fermilab [12], and electron and proton beam measurements at the High-Luminosity LHC [13]. Another type of beam monitor is based on a multichannel plate (MCP) [14, 15] and optical readout, which has been applied in the muon g-2 experiment [16–18] and planned for operation at the China Spallation Neutron Source (CSNS) [19]

Yu Xu and Yun-Song Ning have contributed equally to the project.

This work was supported in part by Fundamental Research Funds for the Central Universities (23xkjc017) at Sun Yat-sen University, the National Natural Science Foundation of China (No. 12075326), and JSPS KAKENHI (No. 22H00139).

✉ Jian Tang
tangjian5@mail.sysu.edu.cn

[1] School of Physics, Sun Yat-sen University, Guangzhou 510275, China

[2] State Key Laboratory of Particle Detection and Electronics, University of Science and Technology of China, Hefei 230026, China

[3] Department of Modern Physics, University of Science and Technology of China, Hefei 230026, China

[4] High Energy Accelerator Research Organization (KEK), Ibaraki 305-0801, Japan

[5] Department of Physics, Imperial College London, London SW72AZ, UK

and HIRFL-CSR [20]. The working principle of the MCP detector is that the injected electrons hit the MCP and are amplified and then recorded by the anode collector board. This design allows measurement of the beam profile of high-intensity beams and can tolerate beam intensities of up to 10^6 μ/s [17].

To achieve individual particle measurements, scintillating fiber detectors have become a good choice [21] owing to their high light yield and fast response. Typically, silicon photomultipliers (SiPMs) are coupled to the scintillating fibers [22] for photon detection. This type of beam profile monitor was used in the R484/R582 experiments at RIKEN [23] and MEG-II experiments at PSI [24]. Furthermore, scintillating fiber detectors can measure the hit time with high accuracy (of up to $\mathcal{O}(1)$ ns) and the deposited energy by counting the photon electrons. Owing to their high-precision characteristics, they can also be used for charged-particle identification in combination with multiple detection systems [25].

The Coherent Muon-to-Electron Transition (COMET) experiment at J-PARC is a next-generation world-leading charged lepton flavor violation experiment that searches for the charged lepton flavor violation process via the coherent neutrinoless muon-to-electron conversion (μ–e conversion) process [26]. The COMET experiment aims to measure the process with a single-event sensitivity of 2.7×10^{-17}, which is four orders of magnitude higher than the current experimental limit given by SINDRUM-II [27]. An 8-GeV bunched proton beam with a 1-MHz pulse structure is slowly extracted from the J-PARC main ring (MR) [28–30]. This beam hits a stopping target and generates the required muon beam for the COMET experiment. One of the key points in the experiment is the high-precision measurement of the COMET muon beam, which requires beam monitoring and measurement during beam commissioning [31].

A muon beam monitor (MBM) was designed to measure and display the COMET muon beams. The goal is to offer a simple and cost-effective detector with compact size and low power consumption that must be easy to operate in a high-radiation environment. In this study, we review the structure and performance of the detector and present test results on high-intensity proton beams and detector performance during COMET phase-α commissioning.

2 Detector system

2.1 Mechanical structure

The core of the MBM is a grid of multi-clad square 1-mm-wide SCSF-3HF scintillating fibers produced by Kuraray [32, 33] coupled at one end to an S13360-1350PE SiPM from Hamamatsu [34], forming a square beam window arranged along the X and Y axes, where the orthogonal axis is perpendicular to the beamline direction. The effective photosensitive area of the selected SiPM is 1.3 mm ×1.3 mm, which matches the cross-sectional area of the scintillating fiber, and the spectral responses of the scintillating fiber and SiPM used are well matched, which can minimize the loss of photons at the transmission interface. The use of square fibers makes the detector response independent of the position of the muon trajectory inside the fiber and minimizes the dead space. The fibers were cut and polished with a heated tungsten steel cutter [35], and silicone grease was coated on the contact end to further improve photon transport efficiency via the fiber–SiPM interface. The fibers were divided into two perpendicular layers spaced 0.8 mm apart, which can cover a beam window of 30 cm × 30 cm. Each layer was made of 128 fibers with a length of 500 mm and 1.3-mm spacing to measure the beam profile in the two orthogonal directions (X and Y).

Scintillating fiber has a total reflection cladding structure and can achieve extremely high light collection efficiency and effectively improve the detection efficiency of the detector. When charged particles go through a scintillating fiber, energy loss occurs through ionization transfer in the scintillating fiber. Ionization energy loss can be estimated using the Bethe–Bloch formula [36]. For organic scintillating materials with densities close to 1 g/cm^3, the corresponding minimum ionization energy loss $\mathrm{d}E/\mathrm{d}x$ is ~200 keV/mm [37], which is acceptable for a high-intensity muon beam with an energy of $\mathcal{O}(10)$ MeV. Simultaneously, the mesh structure can further reduce the average energy loss of the muon beam such that such a detector structure can achieve quasi-noninvasive effects. Using this quasi-noninvasive design and a pure geometric calculation, we observe that 60% of the muons passing through the beam window will be recorded, whereas 16% of the muons will trigger both layers and generate coincident signals. The signals will provide the hit map of the muons and allow characterization of the beam profile.

All the scintillating fibers and their corresponding modules were fixed on an aluminum (Al) plate, and the grid of the scintillating fibers was additionally shielded in a stainless-steel box as a light shield. The beam window on the stainless-steel box was cut off and covered with two layers of Al foil with a thickness of 50 μm. In addition to the grid of fibers shielded in the stainless-steel box, we installed an electronic system on the Al plate, including two electronic modules and one time logic unit (TLU). The two electronic modules were fixed on the two sides of the detector with the SiPMs coupled to the ends of the fibers. The TLU module was fixed at the corner of the Al plate for easy communication with the electronics on both sides. All electronic boards were covered by a resin shell with a metal layer on the surface, which can prevent dust and reduce occasional single-particle flip damage caused by beam–particle scattering to

electronic components. The whole MBM scheme is illustrated in Fig. 1.

2.2 Electronic readout

The electronic readout of the MBM includes two main parts: two electronic modules to read out the signals and upload data to the upper computer and one TLU to synchronize the clock time of the two electronic modules. Each electronic module contains three parts: a SiPM carrier, a front-tend electronics board (FEB), and a data acquisition (DAQ) board. The SiPM carrier contained 128 SiPMs arranged in a 16×8 array and was connected to the FEB with an edge connector. The SiPM transforms photons to photoelectrons and generates a current signal, which is then integrated using a charge-sensitive preamplifier. A pulse signal with a fixed time length and voltage of 3.3 V was produced and processed in the FEB. A power supply module was installed on the SiPM carrier to ensure stable power to all 128 channels. The power supply module was equipped with a built-in temperature compensation system that could adjust the voltage according to the external temperature, thereby improving the stability of the SiPM in different environments.

The FEB board comprises two application-specific integrated circuit (ASIC) chips [38] and a field-programmable gate array (FPGA). The ASIC chip has 64 channels, each of which includes a charge-sensitive preamplifier, a CR–RC shaping circuit, a screener, and other modules. The ASIC chip, which is connected to the TLU in real time through HDMI, amplifies the signals and transmits them to the FPGA. The TLU sends a clock and sampling start signal to the FEB, combining the signal with the timestamp generated by the timer inside the FEB to achieve time synchronization of SiPMs. The FPGA will pack the data and send them to the DAQ board, which transfers the data to the switch, and the data are stored in the computer (or MIDAS Bank) for further processing. We also developed graph interface software that can receive data from the MBM and draw histograms for trigger rates in X and Y directions to monitor the MBM running status in real time.

Owing to the limit of the ASIC chip, the electronics system can only record the time information triggered by the signal while the charge information remains blank. Fortunately, counting and recording the signals that pass through the threshold are sufficient to measure the beam profile and time structure. However, because SiPM characteristics, such as the dark count rate and quantum efficiency, can quite different, the response of the 256 channels of the MBM would also be diverse, which would degrade detector performance. In this case, we carefully designed the electronic readout configuration such that it was possible to modify the threshold of each channel and adjust all channels in uniform responses to the signals. For each channel, the dark count rate was maintained at a low level of ~1 Hz by calibrating the threshold value. Therefore, we expect a high signal-to-noise ratio in the beam-monitoring run.

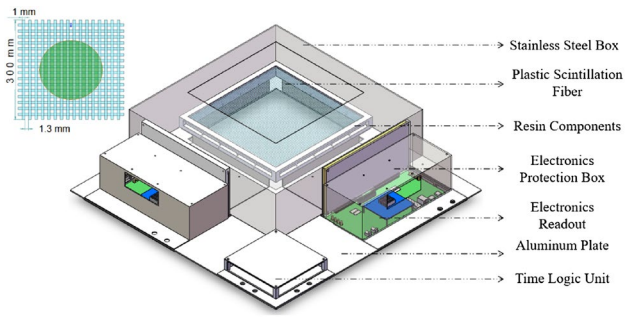

Fig. 1 (Color online) Global setup of the MBM structure. The top left shows the brief grid of scintillating fibers, which in fact covers a beam window of 30 cm × 30 cm

2.3 Validation of detector response

After assembling the MBM, it is necessary to validate the working status of the detector before installing it on the beamline. Therefore, we continuously recorded cosmic-ray data for ~3 h. With this test, we are able to validate two questions: 1. We checked whether the detector can run properly in the whole period; 2. by comparing the collected data with our rough estimates, we checked whether the detector can record the charged particles (cosmic muons) with high efficiency.

For the first purpose, we monitored the working status of the detector in the long run to identify stable detector data without any breaks, as shown by the trigger rate for this period in Fig. 2a.

Second, we analyzed the recorded data and compared them with our expectations. The cosmic-ray muon flux at sea level is ~1 $\mathrm{min}^{-1}\,\mathrm{cm}^{-2}$ [39]; therefore, we must expect ~3 Hz in the MBM. In the actual configuration, the dark count rate was reduced to 1 Hz for each channel by setting an appropriate threshold. Therefore, the trigger rate of all channels in the MBM remains high and at the level of $\mathcal{O}(100)$ Hz, which is approximately two orders of magnitude higher than the naive expectation from cosmic-ray events. Fortunately, in this case, we can switch to coincident measurement and collect cosmic-ray muon events by restricting the X and Y layers triggered within 20 ns, which is 3σ of the fiber decay time. Based on a coincidence time window of 20 ns, the accidental coincidence count rate caused by dark noise in two orthogonal scintillating fibers is 6.6×10^{-4} Hz, which is much lower than the muon count rate of 2.8 Hz based on Monte Carlo simulation results. Therefore, the dark noise frequency is acceptable.

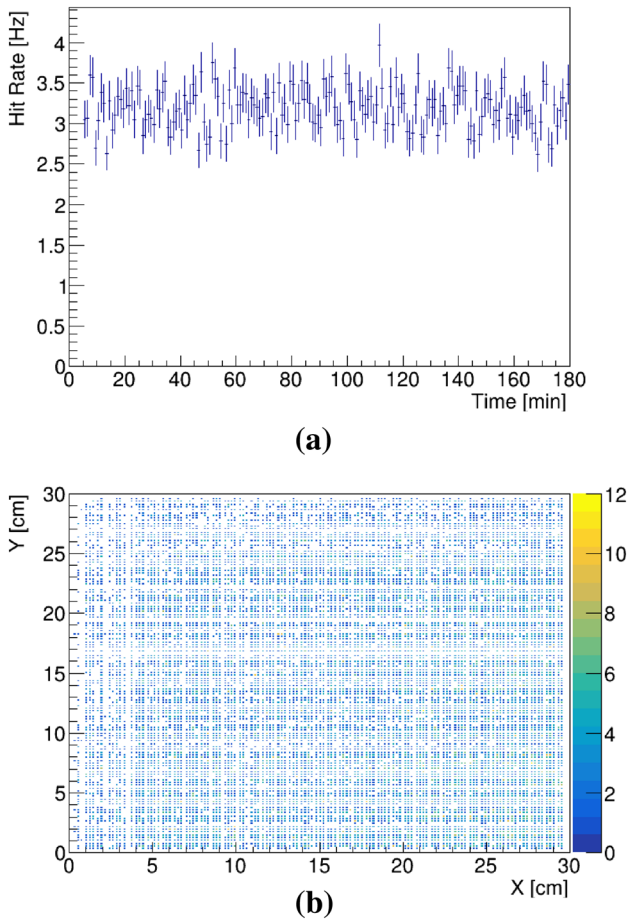

Fig. 2 (Color online) Tests with cosmic-ray muons in the local laboratory. **a** Hit rate of cosmic-ray muons recorded by the MBM detector. **b** Hit map caused by cosmic-ray muons

Finally, satisfactory results are obtained, as shown in Fig. 2. In Fig. 2a, we observe that the coincidence-triggered rate is ~3 Hz, which is consistent with our expected results. In addition, the rate of triggered events was stable in the plot, which indicates the stability of the detector in a relatively long run. In addition, the detector response was almost uniform, indicating good performance for all channels in the MBM (see Fig. 2b). During detector operation, the power was maintained at ~60 W, although it fluctuated slightly during different runs. Based on the above observations, we conclude that the MBM can operate stably for a long time and has the required functionalities to achieve physics objectives.

3 Beam tests

3.1 Proton beam test at the CSNS

To understand the detector response to a high-intensity beam, we conducted a quick beam test using the Associated Proton beam Experiment Platform (APEP) at the CSNS on January 9, 2023 [40]. The detector was installed on the platform on a movable bracket that could move it on the X–Y plane with accurate positioning. Prior to the beam tests, a laser collimator was used to align the beam window to match the center of the beam.

In the APEP setup, the extracted proton beam has a repetition rate of 25 Hz with a 400-μs beam pulse length for each bunch. A suite of degraders was placed downstream of the proton beam window, which allowed us to adjust the proton energy in the range of 10–80 MeV. A collimation system was installed on the beamline to adjust the beam spot size and intensity. Using this system, we can tune the uniform proton beam spot sizes at both the vacuum and air test points from 10 mm × 10 mm to 50 mm × 50 mm. However, the scattering effect of atmospheric molecules on the beam spot in a nonvacuum experimental environment results in an actual beam spot size that is significantly larger than the original size inside the vacuum beamline. For example, the setup of the collimation system of 10 mm × 10 mm would result in a beam spot size of ~70 mm × 70 mm at the air test point [40].

We have two purposes for the beam test. The first objective is to validate the ability of the MBM detector to record the time structure of the beam. Considering the 25-Hz repetition rate of the beam, we selected data within 280 ms, including eight pulses. The time structure is shown in Fig. 3a, and we observe a clear time structure with a regular peak every 40 ms, which is consistent with the 25-Hz beam repetition rate. The other purpose is to validate the ability of the detector to measure the profile of the beam. Therefore, we must draw a two-dimensional plot by selecting the X–Y coincidence events.

However, during the beam test, we found that radiation seriously affected some scintillating fibers operating in the 80-MeV proton beam for a long time, in which almost all channels got triggered continuously at an ultrahigh rate, especially for the previously scanned points. In this case, the true proton events became seriously polluted with the radiation background. Therefore, stricter cuts had to be made to obtain a clean triggered signal:

- The event should be triggered within 10 ns on the X and Y layers.
- The trigger time of the event should be in the range of the beam's spill time.

Using these cuts, we obtained the results shown in Fig. 3b. In the plot, we can observe a clear beam spot at the top center, which is the exact location of the beam arrangement. The size of the beam spot was ~70 mm × 70 mm, which is consistent with the simulation results provided by the CSNS [40]. Based on these tests, we can confirm that the

MBM detector has a good response to the beam particles and can record the timing structure and profile characteristics of the beam quite well.

3.2 COMET phase-α commissioning

To measure the characteristics of proton beams and π and μ production with less ambiguity, which is essential for COMET experiments, the collaborating group proposed a low-intensity beam run called phase-α commissioning. An essential goal of this run was to monitor and measure the properties of muon beams.

The phase-α detector system comprised four subdetectors: the MBM, the straw tube tracker, the range counter (RC), and the proton beam monitor. As the first detector at the backend of the muon beam, the MBM was used to monitor the timing structure and position information of the muon beam and to provide a reference for the downstream detector and beamline quality. The straw tube tracker was installed after the MBM and its task was to measure the position and direction of the injected particles [41]. Because the straw rube tracker is part of the detection system in COMET phase I, phase-α commissioning was used to validate its performance in the beam environment, especially for its electronics system.

At the end of this system is the RC detector, which consists of a series of several plastic scintillators coupled with photomultiplier tubes, aiming to measure the deposited energy and the hit time of the muon events. In addition, the electronic system of the RC detector allows it to record approximately a 10 μs photomultiplier tube waveform; thus, it can measure the decay time of muons decayed in orbit events. The proton beam monitor was installed on a proton beamline and provided real-time proton-beam monitoring. Furthermore, a dedicated beam-masking system was installed upstream of the transport solenoid entrance to study the optics and beam dynamics of the transport solenoid.

3.2.1 Experimental setup

The detector was installed in the COMET Experimental Hall in mid-February 2023. A dedicated 8-GeV bunched proton beam was set up at the J-PARC MR; this beam hits the graphite target and produces a secondary muon beam. This energy proton beam can minimize antiproton pollution and generate sufficient muons to meet physical requirements [26]. The beam spill cycle time was set to 9.2 s, in which the acceleration time and the flat-top time were ~0.6 and ~8.6 s, respectively. The beam power in phase-α commissioning was 0.26 kW. The original plan was to use a 3-T magnetic field to guide the muon beam inside the transmission solenoid. However, in reality, the magnetic field used was only 1.5 T, resulting in a wider spread of the muon beams.

The MBM was installed right after the exit of the transport solenoid with its center aligned with the center of the transport solenoid exit. In addition, during installation, we introduced a trigger signal called "local time'' provided by the RC through an SubMiniature version A (SMA) interface, which was used to reset the time corresponding to the MBM to zero when the event gets triggered. We took data from March 3 to 5 and March 9 to 15 using the secondary muon beam.

3.2.2 Experimental results

For phase-α commissioning, the goal of MBM included two aspects: 1. characterizing the time structure of the muon beam and comparing it with the bunched proton time structure from the J-PARC MR; 2. measuring the muon beam spatial profile to gain a deeper understanding of the beam production and transportation. Moreover, assessing the operational stability of the MBM in harsh environments is essential in the long run.

The timing structure of the muon beam in the COMET is one of the key questions to address. As previously mentioned, the COMET experiment requires a dedicated 8-GeV bunched proton beam that generates the secondary muon beam. In the design of the COMET experiment, the J-PARC MR synchrotron accelerates the protons cycle by cycle. There were nine beam buckets in the MR, with each bucket separated by 586 ns. The beam buckets were not filled completely to obtain the pulsed beam required for the experiment. The MR cycle consists of three bunches (type a) spaced by 1.17 μs and one bunch spaced by 1.76 μs (type b), which are used to effectively reduce the physical background caused by other beam particles. Owing to the low beam intensity in the phase-α commissioning, there are, on average, only 0.02 events recorded by the MBM in one bunch; thus, many events must be superimposed to obtain a plot with a visible structure. However, because of the limited timing resolution from the MR, we were unable to confirm the precise serial number of bunches for the triggered hit. Therefore, the time structure is a superposition of four possibilities (aaab, aaba, abaa, and baaa). Consequently, we expect a time structure with one large peak and six small peaks generated by the misalignment of the beam structure after superposition. The large peak should be spaced at 1.1 μs compared to the small peaks, whereas the small peaks should be separated by 586 ns in the enlarged time window, which is consistent with the MR beam structure. Accumulating data from ~800 runs enabled us to draw the timing structure of the muon beam, as shown in Fig. 4, which meets our expectations.

Another important concern is the muon-beam profile of the COMET. We obtained a two-dimensional profile of the muon beam, as shown in Fig 5. In the actual beam trial operation stage, the measured beam profile is not completely circular as a result of interference from many factors. One of the reasons for this is that the magnetic field in the transport solenoid was set to 1.5 T, which is half of that originally designed in the COMET phase I design. In addition, the detectors in the phase-α commissioning were installed out of the exit of the transport solenoid without any magnetic field and scattering in the air had an effect. Moreover, the beam contains several kinds of charged particles, including e^-, μ^-, and π^-, each of which has a different beam direction. Based on the above analysis, the beam was assumed to be widely spread. This results in different beam spots in the beam profile.

Phase-α commissioning started from March 3 to 13 with a 1.5-T magnetic field. During this period, the muon beam operated stably, and detailed measurements of the time and beam profile structures were conducted. The results are reflected by the stable beam spot, as shown in Fig. 6. To obtain more comprehensive beam profile features, we drew the barycenter of the beam profile and the counting rate of the detector, which also indicates the long-term stability of the detector during the entire phase-α commissioning.

After the successful run in the muon mode, we turned off the magnetic field for several hours and then inverted the direction of the magnetic field and measured the antimuon component in the beam (called the "Mu+ Run,'') to study the beam component and the effect of the magnetic field. In addition, we moved the location of the beam-masking system several times during the Mu+ Run period to validate the beam optics and dynamics in the curved transport solenoid. Figure 6 shows the location of the beam center and the stable trigger rate most of the time. It should be noted that the beam jumps several times after Run 3257, which is caused by the swapping of the magnetic field polarization and the movement of the beam-masking system. In general, the COMET muon beam runs stably, and the MBM reflects the running status of the beam quite well.

To cross-check whether the detector can correctly identify the beam position, we also conducted a coincidence measurement with the RC by selecting the first hits in every event. Consequently, we obtained the hit maps shown in Fig. 7. We can observe a clear hot zone in the plots, which indicates the position of the RC.

We moved the position of the RC to several different locations, allowing us to validate the MBM's response to the beam location. We recorded the relative location of the RC during this period and drew the MBM–RC coincidence beam profile using the corresponding data. In Fig. 7, the beam spot is located at the bottom right (Fig. 7a) and top left (Fig. 7b), which corresponds to RC movement from the bottom right to the top left. Based on these results, we verified the accuracy of the MBM response to the beams.

Table 1 Key specifications of the MBM

Parameter	Value
Time resolution (ns)	1.6
Spatial resolution (mm)	1
Detection area (cm^2)	30×30
Maximum counting rate (kHz)	50
Power consumption (W)	~60

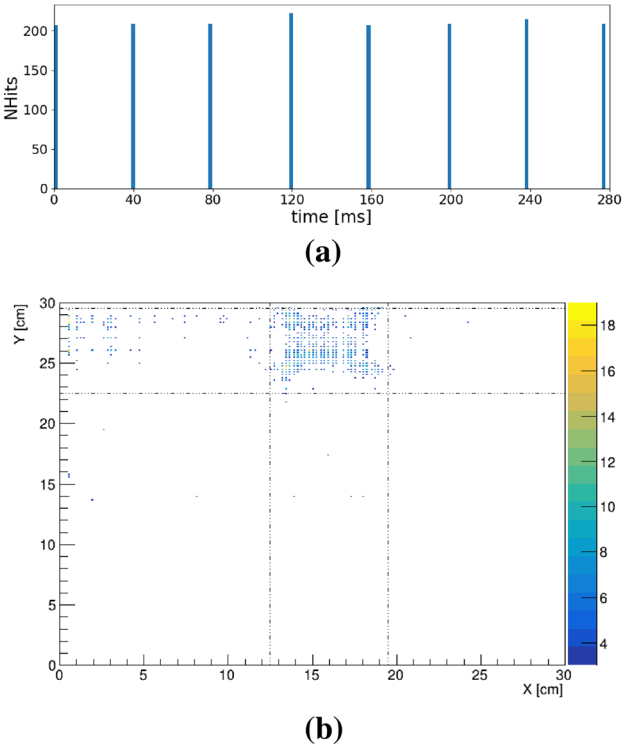

Fig. 3 (Color online) Beam test results with a high-intensity 80-MeV proton beam at CSNS. **a** Timing structure of the proton beam at CSNS. **b** Beam spot during CSNS beam tests

4 Summary and outlook

The first complete MBM with 1-mm-wide scintillating fibers and *X*–*Y* readout using the SiPM was designed and used for COMET phase-α commissioning. Some key specifications are summarized in Table 1.

We validated the monitoring system with cosmic-ray muons in a local laboratory and checked the MBM functionalities through several rounds of beam tests, including the timing structure and beam profile of the muon and proton beams. The performance of the MBM is good. The current

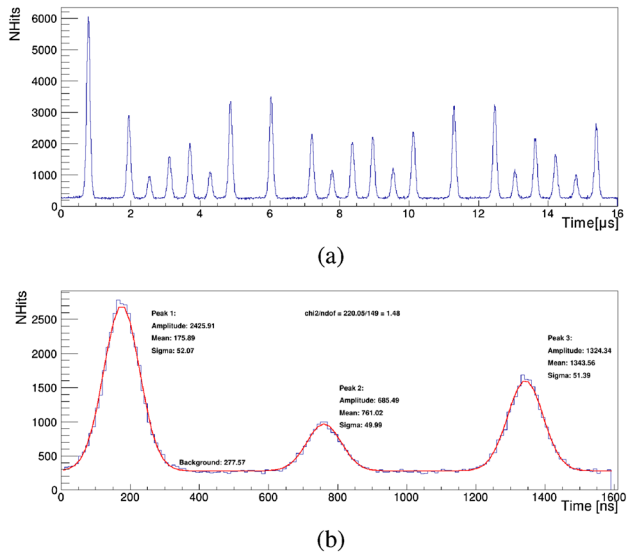

Fig. 4 Monitoring the timing structure of the muon beam during phase-α commissioning. **a** Overview of the timing structure. **b** Details of the peak fittings in a short time window

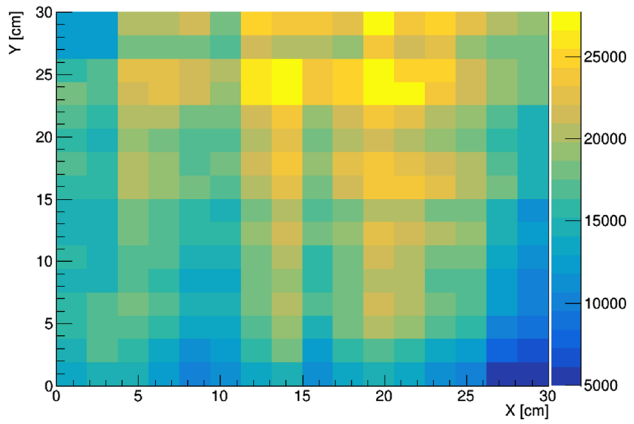

Fig. 5 (Color online) Two-dimensional muon beam profile during COMET phase-α commissioning

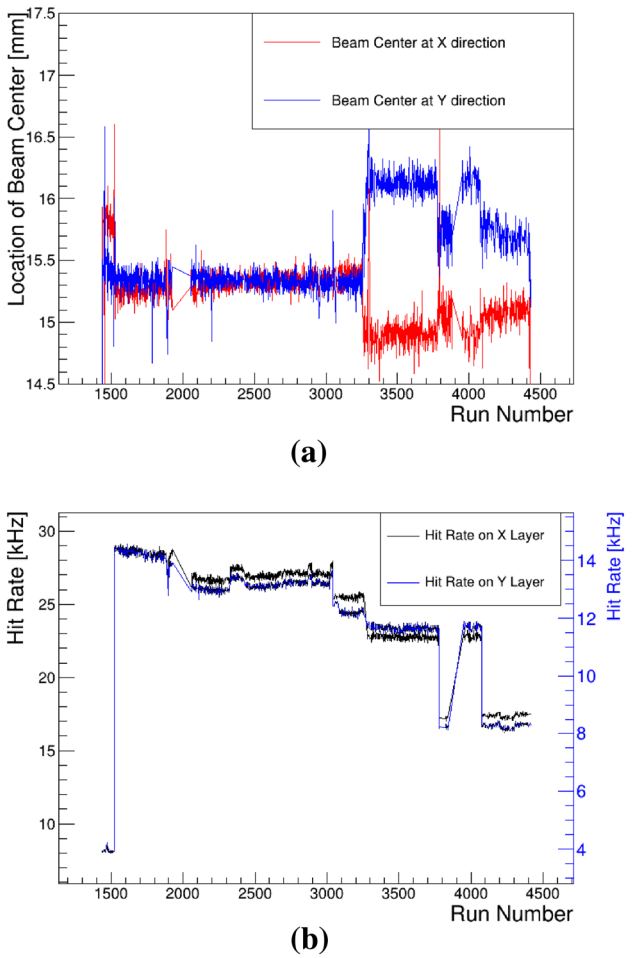

Fig. 6 Long-term stability of the muon beam. **a** Change of center location during the beam time. **b** Change in hit rates during the beam time

experience in the development of the MBM for COMET experiments may facilitate other similar beam instrumentation at various accelerator centers.

From the COMET phase-α commissioning experience, we consider a further upgrade of the MBM to satisfy the requirements for operation in the phase I period. Compared to the current phase-α, the beam intensity in phase I will be increased by approximately three orders of magnitude. Upgrading the electronic readout of the detector is needed to avoid pile-up events, including an upgrade of electronics to record both charge and time information and a more powerful DAQ system for much higher trigger rates. Moreover, as the backend detector needs to be installed inside the detector solenoid in the phase I experiment and the detector solenoid provides a 1-T magnetic field environment [42], the electronic parts to collect SiPM signals need to be placed outside the detector solenoid to avoid damage caused by the high-magnetic-field environment. However, the location of the electronic components also requires consideration of the strong radiation effect caused by neutrons in the harsh environments outside the solenoid. Therefore, it will be a tough task to strengthen the radiation hardness of the electronics to avoid single-event upset. Although pinpointing the exclusion limit or claiming the discovery of new physics can be challenging, efforts to achieve breakthroughs should be taken as a means to drive cutting-edge technologies with fundamental science.

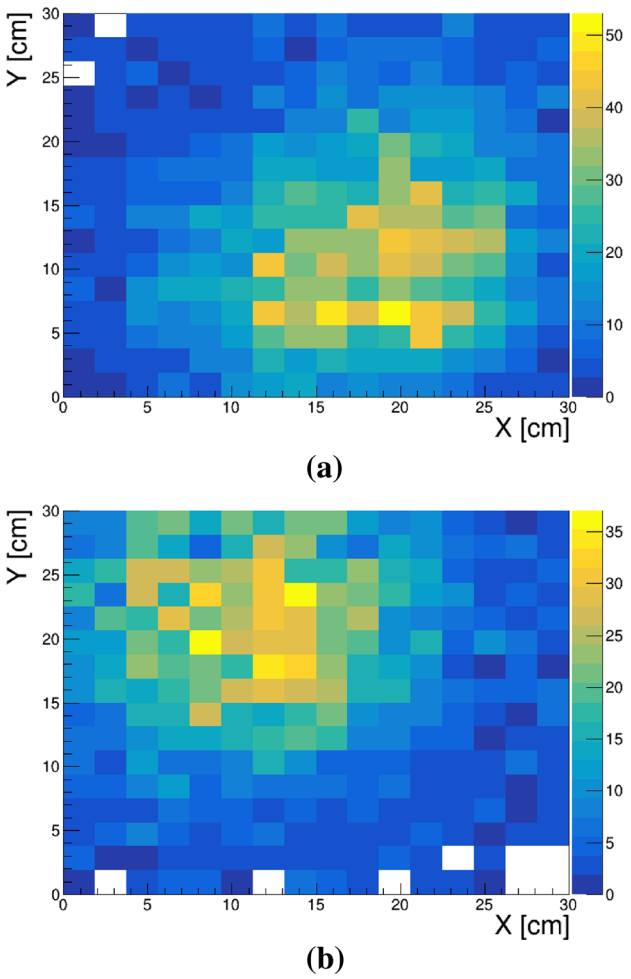

Fig. 7 (Color online) MBM–RC coincidence hit maps for when the RC is **a** located in the bottom right and **b** moved to the top left

Acknowledgements We thank J-PARC as the host laboratory and the COMET phase-α team for their support. We are grateful to the CSNS accelerator group for providing a stable beam during the two rounds of tests. We would also like to thank Prof. Yi Liu from Zhengzhou University for his contribution to data acquisition.

Author contributions All authors contributed to the study conception and design. Material preparation, data collection and analysis were performed by Yu Xu, Yun-Song Ning, Zhi-Zhen Qin and Yao Teng. The first draft of the manuscript was written by Yu Xu and Yun-Song Ning. All authors commented on previous versions of the manuscript. All authors read and approved the final manuscript.

Data availability The data that support the findings of this study are openly available in Science Data Bank at https://cstr.cn/31253.11.sciencedb.16842 and https://www.doi.org/10.57760/sciencedb.16842.

Declarations

Conflict of interest Chang-Qing Feng is an editorial board member for Nuclear Science and Techniques and was not involved in the editorial review, or the decision to publish this article. All authors declare that there are no conflict of interest.

References

1. J. He, Y.F. Sui, Y. Li et al., Design and fabrication of button-style beam position monitors for the HEPS synchrotron light facility. Nucl. Sci. Tech. **33**, 141 (2022). https://doi.org/10.1007/s41365-022-01126-7
2. H.L. Wang, Z. Wang et al., Design and tests of the prototype a beam monitor of the CSR external target experiment. Nucl. Sci. Tech. **33**, 36 (2022). https://doi.org/10.1007/s41365-022-01021-1
3. K. Suzuki, S. Aoki, A. Ariga et al., Measurement of the muon beam direction and muon flux for the T2K neutrino experiment. Progr. Theor. Exp. Phys. **2015**, 053C01 (2015). https://doi.org/10.1093/ptep/ptv054
4. Z. Li, P. Cheng, H. Geng et al., Physics design of an accelerator for an accelerator-driven subcritical system. Phys. Rev. ST Accel. Beams **16**, 080101 (2013). https://doi.org/10.1103/PhysRevSTAB.16.080101
5. Y. Zhang, J.X. Wu, G.Y. Zhu et al., Capacitive beam position monitors for the low-β beam of the Chinese ADS proton linac. Chin. Phys. C **40**, 080101 (2016). https://doi.org/10.1088/1674-1137/40/2/027003
6. S. Walston, S. Boogert, C. Chung et al., Performance of a high resolution cavity beam position monitor system. Nucl. Instrum. Methods A **578**, 1–22 (2007). https://doi.org/10.1016/j.nima.2007.04.162
7. T. Suwada, N. Kamikubota, H. Fukuma et al., Stripline-type beam-position-monitor system for single-bunch electron/positron beams. Nucl. Instrum. Methods A **440**, 307–319 (2000). https://doi.org/10.1016/S0168-9002(99)00960-2
8. I. Yamada, M. Wada, K. Moriya et al., High-intensity beam profile measurement using a gas sheet monitor by beam induced fluorescence detection. Phys. Rev. Accel. Beams. **24**, 042801 (2021). https://doi.org/10.1103/PhysRevAccelBeams.24.042801
9. Y. Liu, Z. Fang, K. Futatsukawa et al., Progress of J-PARC LINAC Commissioning, in *10th International Particle Accelerator Conference* (2019), p. TUPTS027. https://doi.org/10.18429/JACoW-IPAC2019-TUPTS027
10. J. Kamiya, Y. Hikichi, M. Kinsho et al., Non-destructive 2-D beam profile monitor using gas sheet in J-PARC LINAC. J. Phys. Conf. Ser. **1067**, 072006 (2018). https://doi.org/10.18429/JACoW-IPAC2018-WEPAL014
11. A. Miura, N. Ouchi, H. Oguri et al., Design and delivery of beam monitors for the energy-upgraded linac in J-PARC. J. Korean Phys. Soc. **66**, 364–372 (2015). https://doi.org/10.3938/jkps.66.364
12. P. Snopok, A. Bashyal, T. Rehak et al., NuMI beam muon monitor data analysis and simulation for improved beam monitoring. in *3rd North American Particle Accelerator Conference (NAPAC2019)* (2019), p. WEPLM06. https://doi.org/10.18429/JACoW-NAPAC2019-WEPLM06
13. A. Salehilashkajani, M. Ady, N.S. Chritin et al., Non-invasive beam profile monitoring for the HL-LHC hollow electron lens, in *JACoW, IPAC*, vol. 2021 (2021), pp. 884–887. https://doi.org/10.18429/JACoW-IPAC2021-MOPAB279
14. B. Kim, S. Bae, H. Choi et al., Development of a microchannel plate based beam profile monitor for a re-accelerated muon beam. Nucl. Instrum. Methods A **899**, 22–27 (2018). https://doi.org/10.1016/j.nima.2018.05.014
15. T. Sudjai, J.S. Lapington, S.A. Leach, Picosecond imaging at high spatial resolution using TOFPET2 AISC v2d and microchannel plate detector, in *JINST*, vol. 17 (2022), p. C09016. https://doi.org/10.1088/1748-0221/17/09/C09016
16. F. Jegerlehner, The Muon g-2 in Progress. Acta Phys. Polon. B **49**, 1157 (2018). https://doi.org/10.5506/APhys-PolB.49.1157

17. G.P. Razuvaev, S. Bae, H. Choi et al., The low energy muon beam profile monitor for the muon g−2/EDM experiment at J-PARC, in *JINST*, vol. 12 (2017), p. C09001. https://doi.org/10.1088/1748-0221/12/09/C09001
18. G. Razuvaev, Y. Cho, S. Choi et al., Development of the CsI(Tl) muon beam profile monitor for the muon $g-2$/EDM experiment at J-PARC. EPJ Web Conf. **212**, 01008 (2019). https://doi.org/10.1051/epjconf/201921201008
19. Y. Zhang, S. Fu, Y. Ruan et al., Ionization beam profile monitor designed for CSNS, in *Particle Accelerator Conference (PAC 09)* (2010), p. TH5RFP022
20. H.M. Xie, K.W. Gu, Y. Wei et al., A noninvasive ionization profile monitor for transverse beam cooling and orbit oscillation study in HIRFL-CSR. Nucl. Sci. Tech. **31**, 40 (2020). https://doi.org/10.1007/s41365-020-0743-7
21. A. Stoykov, R. Scheuermann, T. Prokscha et al., A scintillating fiber detector for muon beam profile measurements in high magnetic fields. Nucl. Instrum. Methods A **550**, 212–216 (2005). https://doi.org/10.1016/j.nima.2005.04.089
22. R. Rossini, R. Benocci, R. Bertoni et al., Characterisation of muon and proton beam monitors based on scintillating fibres with a SiPM read-out. Nucl. Instrum. Methods A **1046**, 167684 (2023). https://doi.org/10.1016/j.nima.2022.167684
23. M. Bonesini, R. Bertoni, F. Chignoli et al., The construction of the Fiber-SiPM beam monitor system of the R484 and R582 experiments at the RIKEN-RAL muon facility, in *JINST*, vol. 12 (2017), p. C03035. https://doi.org/10.1088/1748-0221/12/03/C03035
24. G. Dal Maso, F. Barchetti, M. Francesconi et al., Beam monitoring detectors for high intensity muon beams. Nucl. Instrum. Methods A **1047**, 167739 (2023). https://doi.org/10.1016/j.nima.2022.167739
25. E.O. Cohen, E. Piasetzky, Y. Shamai et al., Development of a scintillating-fiber beam detector for the MUSE experiment. Nucl. Instrum. Methods A **815**, 75–82 (2016). https://doi.org/10.1016/j.nima.2016.01.044
26. R. Abramishvili, R.R. Akhmetshin, A. Allin et al., COMET phase-I technical design report. PTEP **2020**, 033C01 (2020). https://doi.org/10.1093/ptep/ptz125
27. W.H. Bertl, R. Engfer, E.A. Hermes et al., A Search for muon to electron conversion in muonic gold. Eur. Phys. J. C **47**, 337–346 (2006). https://doi.org/10.1140/epjc/s2006-02582-x
28. M. Tomizawa, Y. Arakaki, T. Kimura et al., Slow extraction operation at J-PARC main ring, in **JACoW. HB2021, THDC1** (2022). https://doi.org/10.18429/JACoW-HB2021-THDC1
29. K. Oishi, Y. Fujii, Y. Fukao et al., Detector systems development for Inter-bunch extinction measurements at the 8 GeV slow extracted pulsed proton beam for the COMET experiment at J-PARC, in **PoS. NuFact2021** (2022), p. 216. https://doi.org/10.22323/1.402.0216
30. K. Noguchi, Y. Fujii, Y. Fukao et al., Extinction measurement at J-PARC MR with slow-extracted pulsed proton beam for COMET experiment, in **PoS. NuFact2021** (2022), p. 104. https://doi.org/10.22323/1.402.0104
31. M. Cerv, P. Sarin, H. Pernegger et al., Diamond detector for beam profile monitoring in COMET experiment at J-PARC. JINST **10**, C06016 (2015). https://doi.org/10.1088/1748-0221/10/06/C06016
32. M. Gandini, I. Villa, M. Beretta et al., Efficient, fast and reabsorption-free perovskite nanocrystal-based sensitized plastic scintillators. Nat. Nanotechnol. **15**, 1–7 (2020). https://doi.org/10.1038/s41565-020-0683-8
33. P. Zhmurin, Y. Gurkalenko, V. Pereymak et al., Plastic scintillators with the improved radiation hardness level, in *Springer Proc. Phys.*, vol. 09 (2019), pp. 125–145. https://doi.org/10.1007/978-3-030-21970-3_10
34. V. Kitsmiller, C. Campbell, T. O'Sullivan, Optimizing sensitivity and dynamic range of silicon photomultipliers for frequency-domain near infrared spectroscopy. Biomed. Opt. Express **11**, 08 (2020). https://doi.org/10.1364/BOE.401439
35. D. Sáez-Rodríguez, K. Nielsen, O. Bang et al., Simple room temperature method for polymer optical fibre cleaving. J. Light Wave Technol. **33**, 4712–4716 (2015). https://doi.org/10.1109/JLT.2015.2479365
36. R.L. Workman, V.D. Burkert, V. Crede et al., Review of particle physics. Prog. Theor. Exp. Phys. **2022**, 083C01 (2022). https://doi.org/10.1093/ptep/ptac097
37. R.C. Ruchti, The use of scintillating fibers for charged-particle tracking. Ann. Rev. Nucl. Part. Sci. **46**, 281–319 (1996). https://doi.org/10.1146/annurev.nucl.46.1.281
38. Y. Pu, Y. Zeng, Y. Zhao et al., Design and implementation of testing system of the readout asic-mapmt_v10 for scintillator neutron detector. Nucl. Tech. **38**, 402 (2015). https://doi.org/10.11889/j.0253-3219.2015.hjs.38.020402. (**in Chinese**)
39. L. Bonechi, R. D'Alessandro, A. Giammanco, Atmospheric muons as an imaging tool. Rev. Phys. **5**, 100038 (2020). https://doi.org/10.1016/j.revip.2020.100038. [arXiv:1906.03934 [physics.ins-det]]
40. Y. Liu, H. Jing, L. Huang et al., Physical design of the APEP beam line at CSNS. Nucl. Instrum. Methods A **1042**, 167431 (2022). https://doi.org/10.1016/j.nima.2022.167431
41. H. Nishiguchi, H. Danielsson, E. Hamada et al., Vacuum-compatible, ultra-thin-wall straw tracker; detector construction, thinner straw R and D, and the brand-new graphite-straw development. Nucl. Instrum. Methods A **1042**, 167373 (2022). https://doi.org/10.1016/j.nima.2022.167373
42. N. Sumi, M. Yoshida, M. Iio et al., Construction and commissioning status of the superconducting magnets for COMET phase-I experiment at J-PARC. IEEE Trans. Appl. Supercond. **33**, 4500205 (2023). https://doi.org/10.1109/TASC.2023.3247679